Open inventories of rainfall-triggered landslides

Rachel (Soobitsky) Vershel[1,3], Jessica Sutton[2,3], Thomas Stanley[2,3], Pukar Amatya [2,3], and Dalia Kirschbaum[4]

[1]HBG, Science Systems and Applications, Inc., Greenbelt, MD, USA
[2]GESTAR II, University of Maryland Baltimore County, Baltimore, MD, USA
[3]Hydrological Sciences Laboratory, NASA Goddard Space Flight Center, Greenbelt, MD, USA
[4]Earth Science Division, NASA Goddard Space Flight Center, Greenbelt, MD, USA

*Correspondence: rachel.b.soobitsky@nasa.gov

Running Title: Open inventories of rainfall-triggered landslides

Funding information: This research is supported by the PMM Science Team (NNH21ZDA001N-PMMST, 21-PMMST21-0046) and the NASA Disasters Program (NNH18ZDA001N-DISASTERS, 18-DISASTER18-0022).

Data availability statement: The landslide inventory is available in Figshare (https://doi.org/10.6084/m9.figshare.26972467)

Dataset Details:
Landslide Inventory
Identifier: https://doi.org/10.6084/m9.figshare.26972467
Creator: Rachel (Soobitsky) Vershel, Pukar Amatya
Dataset correspondence: rachel.b.soobitsky@nasa.gov
Title: Open inventories of rainfall-triggered landslides, new landslide events
Publisher: Figshare
Publication year: 2025
Resource type: Landslide inventory
Version: 1

Abstract

Landslide inventories support both post-event response and predictive model evaluation, but it remains challenging to create public, current, comprehensive, and accurate landside inventories. In response to this need, thousands of rainfall-triggered landslides were mapped and organized within the National Aeronautics and Space Administration's Cooperative Open-Online Landslide Repository (COOLR), which contains over 11,000 landslide reports from the Global Landslide Catalog. Recently, 22 inventories containing thousands of rainfall-triggered landslides have been added to COOLR, which was re-organized to better accommodate large landslide inventories. All the data are available on the "Landslide Viewer" web application, which also shows referenced and imported landslide inventories from other researchers. The new inventories are each connected to a landslide-triggering rainfall event, and therefore their date of occurrence was usually known. Landslide events were found by searching through credible sources or due to an external request for support during a disaster response. In either case, high-resolution imagery was utilized to digitize the landslides in the region. The resulting data can be used for various purposes, such as model training and validation. To demonstrate their potential, satellite precipitation was analyzed with reference to the new inventories. The precipitation analysis highlights the potential of daily satellite precipitation estimates in areas with limited ground precipitation observations. Some of the heavy precipitation events were underestimated, but many were captured and could inform future landslide hazard assessment.

Keywords: Landslides, Landslide Inventory, COOLR, Satellite, Precipitation

1. Introduction

The accuracy and composition of landslide inventories varies widely. Creating a global, up-to-date, comprehensive, and accurate landside inventory is a challenge, due to varying collection methods, numerous types and causes of landslides, and the large effort required to create a global inventory of any kind. The National Aeronautics and Space Administration (NASA) recently updated its Cooperative Open Online Landslide Repository (COOLR) to include a series of major landslide events.

Landslide mapping can be accomplished using manual or automated methods. In manual mapping, a human digitizes landslides via visual interpretation of imagery, which tends to produce fewer false positives. However, this method can be labor- and time-intensive, and the quality is variable and dependent on the experience of the human analyst. Automated mapping involves the use of supervised or unsupervised classification techniques to detect landslides from satellite imagery. Pixel-based (Nichol and Wong, 2005; Borghuis *et al.*, 2007; Parker *et al.*, 2011; Burrows *et al.*, 2019, 2020; Jung and Yun, 2020), Object-based (Martha *et al.*, 2010, 2016; Lu *et al.*, 2011; Stumpf and Kerle, 2011; Hölbling *et al.*, 2012, 2015; Amatya *et al.*, 2019, 2021a, 2021b; Adriano *et al.*, 2020; Esposito *et al.*, 2020; Comert, 2021) and deep-learning based (Ghorbanzadeh *et al.*, 2019; Sameen and Pradhan, 2019; Meena *et al.*, 2021; Nava *et al.*, 2022; Bhuyan *et al.*, 2023) methods have been used extensively for landslide mapping. These methods can quickly map large areas but can produce more false positives, requiring further corrections (Li *et al.*, 2014). In this paper, we utilized both manual mapping and an automated landslide mapping approach, called Semi-Automatic Landslide Detection (Amatya *et al.*, 2021a, 2021b).

Although many individual landslide inventories have been published, relatively few compilations of multiple inventories have been made publicly available. Institutional restrictions on data republication are probably an important limiting factor, but the labor and computing costs associated with maintaining up-to-date repositories may also be significant. A common challenge to these efforts is standardization of diverse datasets (Grignon *et al.*, 2004). Due to the challenge of producing a single landslide inventory at scale, national landslide inventories often represent a compilation across multiple pre-existing inventories (Devoli *et al.*, 2007; Trigila *et al.*, 2010; Mirus *et al.*, 2020), and these are sometimes made openly available. Fewer examples are available at the international level. Sometimes multiple inventories may be compiled to produce an open landslide susceptibility map or other product (Günther *et al.*, 2014; Wilde *et al.*, 2018), but without publishing the merged inventory (Herrera *et al.*, 2018). The pre-eminent example of an open repository of multiple landslide inventories, a collection of earthquake-induced landslides is redistributed through the U.S. Geological Survey ScienceBase platform (Tanyaş *et al.*, 2017). This database is intended to enhance sharing of information across the research community, as well as improving the estimation of impacts from future earthquakes. In this paper, we describe updates to COOLR, another global repository of landslide data, including the production of dozens of new landslide inventories.

The new inventories correspond to 22 rainfall events that occurred in the years 2019-2023 and contain over 15,000 landslides (**Figure 1**). The new point-based inventories are hosted within COOLR and can be viewed and downloaded on NASA's Landslide Viewer (http://www.landslides.nasa.gov/viewer). COOLR already contains the Global Landslide Catalog (GLC), a large inventory of rainfall-triggered landslides that have been recorded by news media or other sources (Li *et al.*, 2014; Kirschbaum *et al.*, 2015). The new inventories can be used for training or validating landslide predictive models, such as the Landslide Hazard for Situational Awareness (LHASA) model (Stanley *et al.*, 2021). In addition, these data could be used for evaluating the connection between landslide events and satellite precipitation datasets, an example explored in this paper.

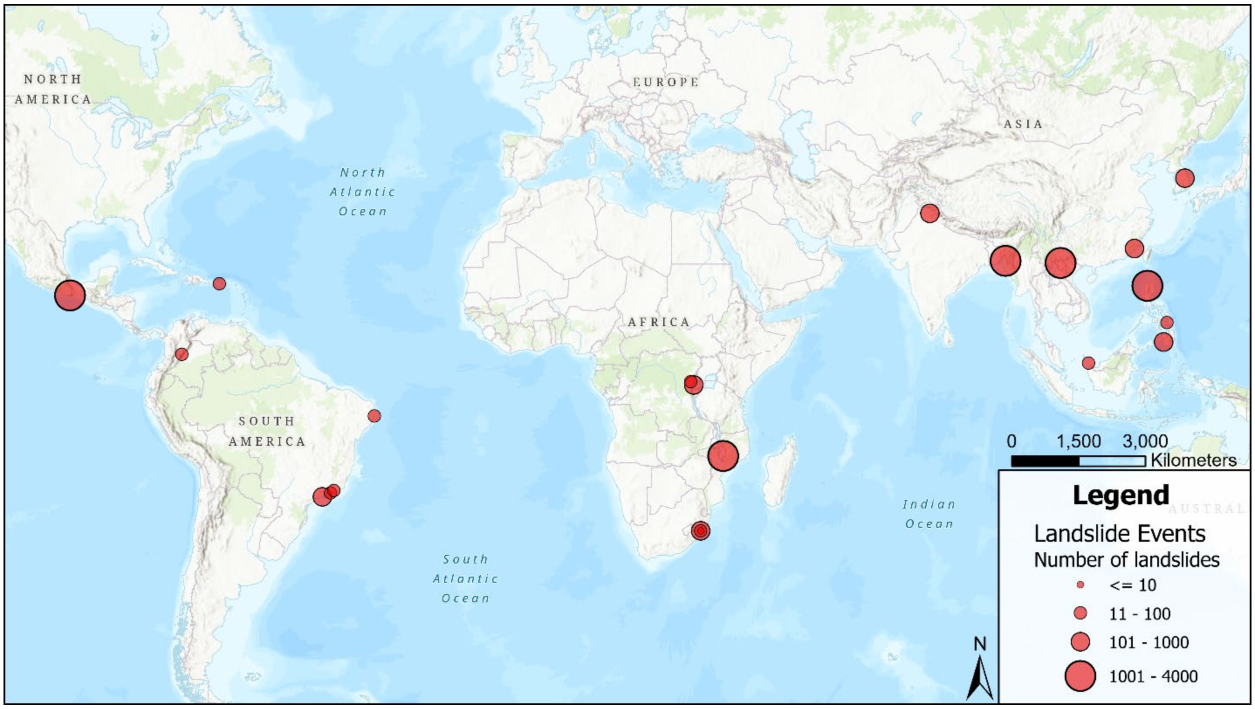

Figure 1. Locations of the new landslide inventories.

2. Methodology

2.1. Landslide Mapping

2.1.1. Information sources

Multiple sources of information fed the digitization of landslide events. Sometimes, the NASA Disasters Program (https://appliedsciences.nasa.gov/what-we-do/disasters) notified our team of a landslide occurrence. The Disasters Program activates the Disasters Response Coordination System (DRCS) (https://appliedsciences.nasa.gov/what-we-do/disasters/disasters-response-coordination-system) when there is an external request for Earth observation (EO) data or hazard products to support a disaster response. When the DRCS activated for a landslide-related event, the landslide mapping process began. In addition, trustworthy websites such as the International Disasters Charter (IDC) (https://disasterscharter.org) and Floodlist (https://floodlist.com/) were used to find rainfall-triggered landslide events to digitize. Both sources were filtered by hazard type, location, and date. The overall methodology and decision process for mapping landslide events is shown in **Figure 2**.

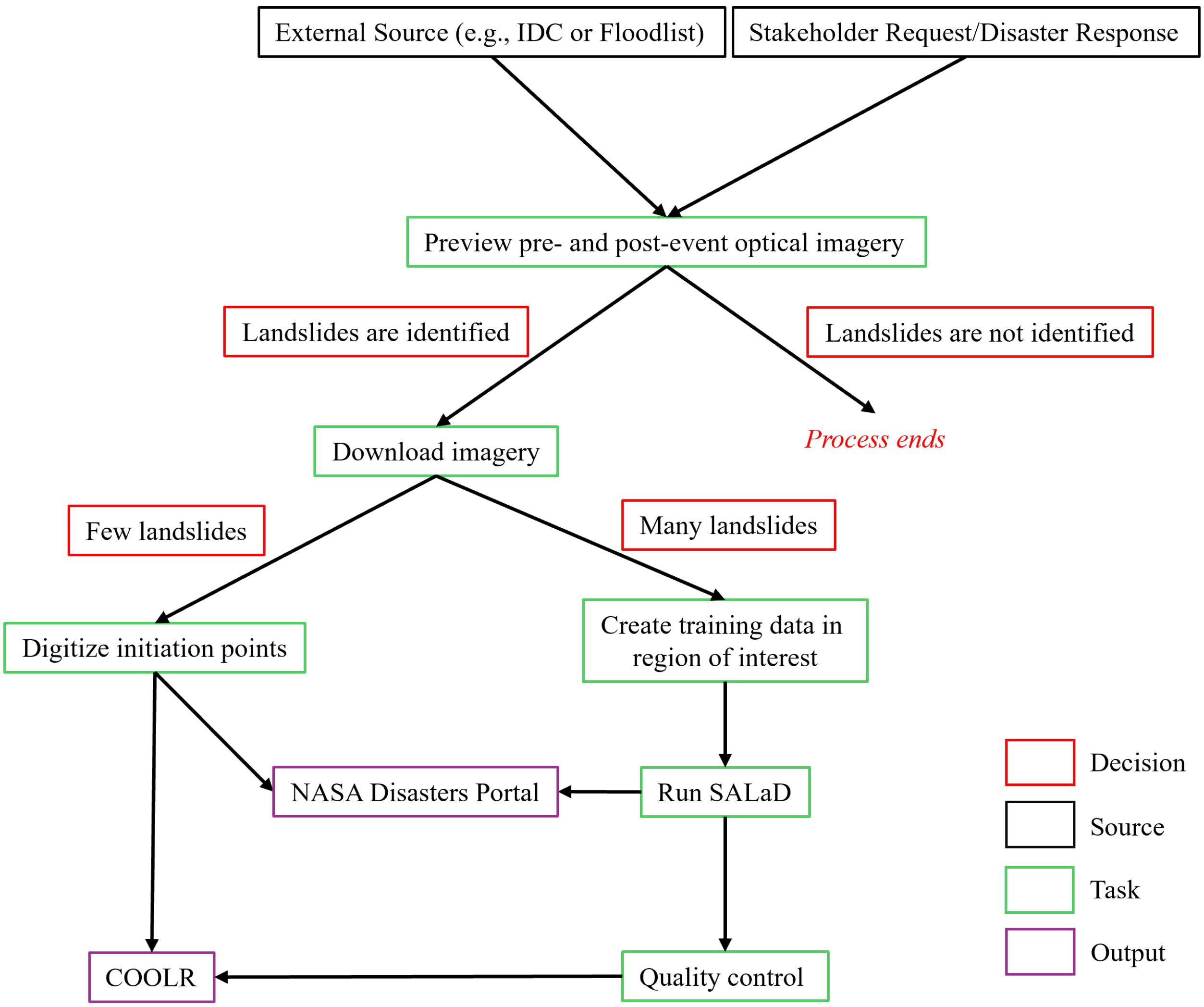

Figure 2. Flowchart showing each step of the landslide inventory creation process.

2.1.1. Data

To precisely map individual landslides, a surface-reflectance product with 4-bands (Red, Green, Blue and Near-Infrared) from PlanetScope (Planet Team, 2017) was used. The imagery was available through the NASA Commercial Satellite Data Acquisition (CSDA) Program (https://earthdata.nasa.gov/esds/csdap). The PlanetScope imagery had a 3-meter daily resolution. The high temporal frequency gave the greatest chance of finding a cloud-free image from both before and after each rainfall event, which helped attribute each landslide to the rainfall event.

If landslides were mapped for a disaster response, it was often difficult to find a post-event cloud-free image as some areas may remain cloudy for many days. In those cases, imagery sources were checked daily until clear imagery became available. In some regions, it was often hard to find a cloud-free image from within a narrow time window before and after the event. This phenomenon can reduce the overall precision of the product, but the date of the imagery used for digitization was provided in the data attributes to provide context for each mapped inventory. Errors were possible in both manual and automatic mapping. False negatives might have occurred if the area of interest excluded nearby landslides or if landslides were overlooked due to spectral characteristics. False positives could have occurred due to unrelated changes or damage to the landscape that looked like a landslide. Finally, false positives and false negatives were manually corrected during the quality assurance/quality control (QAQC) process.

2.1.2 Manual Mapping

When NASA was alerted to a potential landsliding event, the first step was to download clear pre-event and post-event imagery. The threshold for determining a "clear" image was 30% cloud cover, but we manually selected the best available image for mapping each landslide event. Once both were available, the clear pre-event imagery was compared with clear post-event imagery. If new landslides were identified, the next step was to determine whether manual digitization or machine learning would be used to map landslides. Most inventories were manually digitized. The manual process to digitize landslides was comprised of visualizing and comparing the pre- and post- event imagery in Esri ArcGIS Pro software. The region of interest was visually inspected to capture as many landslides as possible, with closer attention paid to steeper terrain, especially near streams and in forested areas. A point was placed at the suspected initiation zone of each landslide based on the topography of the region. We decided to map the landslides as points instead of polygons because adding a point at the suspected initiation zone is much faster, enabling us to map many landslides in a short amount of time. To ensure we captured all the landslides in the given region, we reviewed the entire administrative district mentioned in the source for the event (typically a county). If no administrative district was mentioned in the source, we reviewed the imagery at least 25 kilometers out from the furthest landslide found in all directions. When each new inventory was completed, it was shared with the requester for the ongoing disaster response and published within COOLR.

2.1.3. Semi-Automatic Landslide Detection (SALaD) system

When we identified an event that seemed too large to manually map, the Semi-Automatic Landslide Detection (SALaD) algorithm was utilized (Amatya *et al.*, 2021b). SALaD uses object-based image analysis and machine learning to automatically map landslides. To ensure that only landslides induced by that rainfall event were mapped, a change detection-based version of SALaD called SALaD-CD (Amatya *et al.*, 2021b) was used. First, pre- and post-event imagery of the area of interest was downloaded. Next, training data was created to represent a sample of landslides in the region of interest, to improve accuracy. Pre- and post-event imagery was used to generate metrics that highlight change such as Normalized Difference Vegetation Index (NDVI) difference, Principal Component Analysis (PCA) and Independent Component Analysis (ICA). The post-event image was segmented to create objects (Comaniciu and Meer, 2002). The mean of NDVI difference, PCA and ICA of each object was used for landslide classification using a Random Forest (RF) model (Breiman, 2001). Once SALaD-CD finished running, either the output was posted with only a few corrections (mostly removing clouds) or a full QAQC was performed before publishing to COOLR. SALaD-CD outputs landslide polygons. In this case, the polygons were converted to initiation points before QAQC, because performing corrections was faster on points than on more complex polygons. The initiation point was assumed to be the highest elevation in the landslide polygon boundary, based on the NASA Digital Elevation Model (NASA JPL, 2020). Missing landslide initiation points due to amalgamation of landslides while generating polygons were added manually. If the mapping was performed due to a request from an external organization working a hazard response in real-time, the output of SALaD-CD was shared as soon as possible. After the immediate response, each inventory was reviewed before it was ingested into COOLR.

2.2. COOLR Incorporation

All of the newly digitized landslide event inventories were added to COOLR, NASA's landslide database, which is displayed within NASA's Landslide Viewer. However, the pre-existing repository structure did not differentiate between event-based and report-based landslide inventories. Previously, COOLR contained two layers that hosted all the landslide data: a point layer and a polygon layer. These contained landslides reported by citizen scientists (Juang *et al.*, 2019), landslides recorded in the GLC by NASA staff (Dandridge *et al.*, 2023), and inventories that were shared by external researchers. The database structure had been developed around the GLC, a report-based inventory. For this reason, the schema was not ideal for representing event-based inventories, which can have thousands of spatially precise landslide points per event. To better represent the new inventories, COOLR was updated to contain four layers: event-based layers in point and polygon format, and report-based layers in point and polygon format.

Both the event- and report-based layers contain external landslide inventories with the attributes updated to match the COOLR schema. External inventories contained within COOLR will be identified as such within the "Event Title" or "Imported Event Source Catalog" fields. If an external inventory was published via an online service, the service was added directly to Landslide Viewer as a separate layer. These inventories can be viewed in Landslide Viewer within the "map layers" list under "External Landslide Catalogs (Referenced)". The goal was to have Landslide Viewer as comprehensive as possible for all public-facing landslide inventories.

The attributes within the event- and report-based landslide inventories differ slightly and can be seen in **Table 1** below.

Attribute	Description
Event Title (events, reports)	A title often describing the method for mapping the event, the location, and the date of the event.
Event Date (events, reports)	The date the landslide(s) most likely occurred.
Event Time (approximate) (events, reports)	The approximate time the landslide(s) occurred.
Name of Information Source (events, reports)	The source of information for an event, such as a citation for the landslide inventory, a news article, etc.
Link to Information Source (events, reports)	The link to the information source or the publication referenced.
Event ID (events, reports)	A unique identifier assigned to each landslide that will remain constant over time.

Event Description (events, reports)	Describes the landslide event in more detail. Provides context to the situation, such as more details about the location, trigger, etc.
Landslide Trigger (events, reports)	The cause of the landslide, such as earthquake, rainfall, etc.
Event Location (events, reports)	Describes where the landslides occurred geographically.
Associated Storm Name (events, reports)	The name of the storm that caused the landslide, if applicable.
Country Code (events, reports)	The 2-digit country code defined in ISO 3166-1.
Country Name (events, reports)	The full name of the country the landslide(s) occurred in.
Event Comments (events, reports)	Any additional information about the landslide that wasn't captured in the other attributes, especially information on source reliability or process.
Latitude (events, reports)	Latitude of the landslide.
Longitude (events, reports)	Longitude of the landslide.
Landslide Category (reports)	The type of landslide that occurred, such as rockslide, debris flow, mudslide, etc.
Administrative Division (reports)	The administrative division the landslide report is located in.
Closest Gazetteer Point (reports)	The closest geographical dictionary reference point to the reported landslide event.
Distance to Gazetteer Point (reports)	The distance to the closest gazetteer point.
Estimated Size (reports)	Estimated size of the landslide based on the report.
Imported Event Source Catalog (reports)	An abbreviation identifying the relevant landslide inventory. For example, GLC = Global Landslide Catalog.
Imported Event Source ID (reports)	If the landslide report was imported from another source, the ID of that source is listed here.
Landslide Setting (reports)	The environment where the landslide occurred.
Last Edited Date (reports)	The latest date the landslide report was edited within the attribute table.
Link to Photo (reports)	If there is a photo within the landslide report source, it is linked here.
Location Accuracy (reports)	A radius around the reported location within which the landslide is believed to have occurred.
Number of Fatalities (reports)	Estimated number of fatalities associated with the landslide.
Number of Injuries (reports)	Estimated number of injuries associated with the landslide.
Submitted Date (reports)	The date the landslide report was reviewed by NASA and submitted into the public-facing COOLR database.
Citation (events)	The citation for each landslide inventory. Users should reference this field when utilizing the event-based data within COOLR.

Imagery Type for Digitizing (events)	The type of imagery used to manually or automatically digitize the landslide event. Normally, both pre- and post-event imagery is used and noted here.
Method (events)	The type of process used to digitize the landslides, either “manual” or “automatic”.
Satellite Imagery Date Before Event (events)	The date(s) of the satellite image used for digitization pre-event.
Satellite Imagery Date After Event (events)	The date(s) of the satellite image used for digitization post-event.

Table 1. Attribute names and definitions for both the event- and report-based landslide layers in COOLR.

2.3. Satellite Precipitation Analysis

Satellite precipitation enables a global view of extreme rainfall that may be the harbinger of subsequent major landslide events. To evaluate this connection and examine the potential for better detection, the following precipitation analysis was conducted. The analysis used precipitation estimates derived from satellite remote sensors to provide context of the precipitation in the area for each landslide event. Due to the landslides being located in remote areas across the world, precipitation from gauges was sometimes unavailable. Additionally, since the time of day the precipitation event occurred was not documented in the landslide inventory, the precipitation analysis was conducted using daily estimates instead of sub-daily estimates. Daily cumulative precipitation estimates from the Global Precipitation Measurement (GPM) mission were used. Specifically, estimates were from the V07 final run product from the Integrated Mult-satellitE Retrievals for GPM (IMERG) were used for the precipitation analysis and are available at https://gpm1.gesdisc.eosdis.nasa.gov/data/GPM_L3/GPM_3IMERGDF.07/ (Huffman *et al.*, 2023). The multi-satellite precipitation estimate from the product was the only variable used in the analysis. All available daily precipitation estimates at the time of writing, June 1, 2000, through March 31, 2024, were used in the analysis. Once data were downloaded, the overall extent of the bounding area for each landslide event was used to extract precipitation pixels for each day in the study period (**Figure 3**). Each GPM IMERG pixel was 0.1° in spatial resolution. Due to the variations in landslide event bounding area, the number of pixels from GPM IMERG varied. From the daily precipitation pixels extracted, the maximum daily precipitation was determined for each bounding area. This maximum daily cumulative precipitation was used in the analysis to determine the mean recurring interval and percentile rank.

Since the exact date and time of the reported event might not be accurate, and GPM IMERG precipitation estimates are in UTC, precipitation within 5 days before and after the reported event date were analyzed to ensure the precipitation event was fully captured. The maximum daily precipitation value that occurred within 5 days before and after the reported event date was used to define the precipitation amount for each event (**Figure 3**).

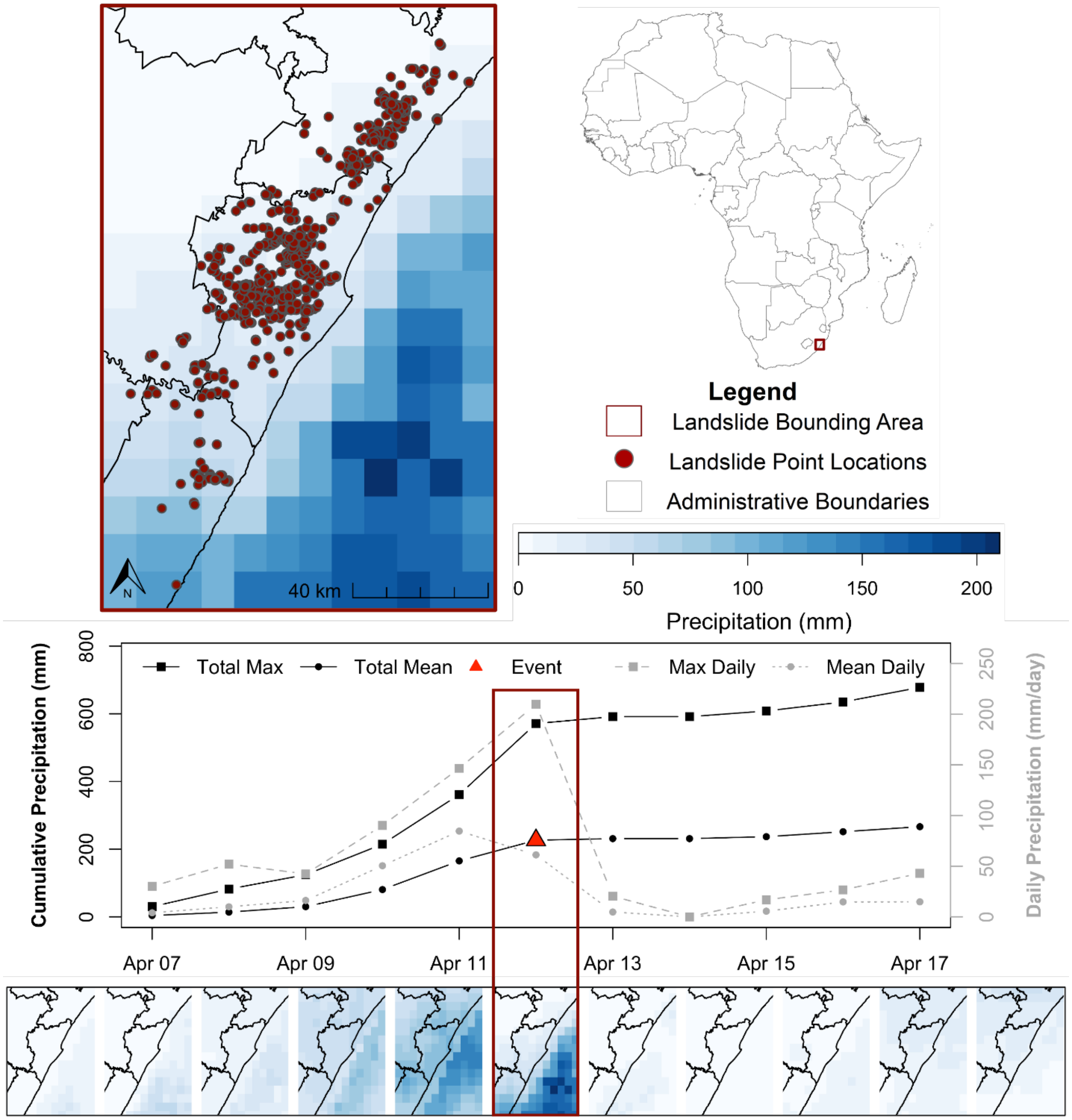

Figure 3. Example of the precipitation analysis completed for each landslide event using the maximum daily precipitation during the ± 5 days of the reported event date. The map and time series shows the analysis for the South Africa (12-April-2022) landslide event. In the map, each red dot represents a mapped landslide location. In the time series plot, the daily maximum precipitation, daily mean precipitation, and cumulative precipitation are shown for each day. The reported landslide event date is highlighted by a red triangle, while the maximum daily precipitation used for the calculation of the recurring interval is highlighted by the dark red rectangle. This example highlights the use of the maximum precipitation that occurred on the reported event date.

The precipitation amount was used in the calculation of the recurring interval. The recurring interval was calculated by averaging the time between precipitation events that had a daily precipitation equal to or higher than the determined amount (Perica *et al.*, 2018). For example, the South Africa (12-April-2022) event had a maximum daily precipitation of 209.9 mm that occurred on the reported event date. The 209.9 mm was the precipitation amount used to determine the number of events that occurred during the IMERG record. The time difference between these events was then averaged to determine the recurring interval. For this amount, there were 3 days that were more than or equal to 209.9 mm within the IMERG record, including the event (**Figure 4**). The average time between the events was 9.87 years. Additionally, the percentile rank of the threshold was calculated for each amount to determine the percentage of days that were less than the event amount. All precipitation analysis was completed using the R software ("R Core Team," 2024).

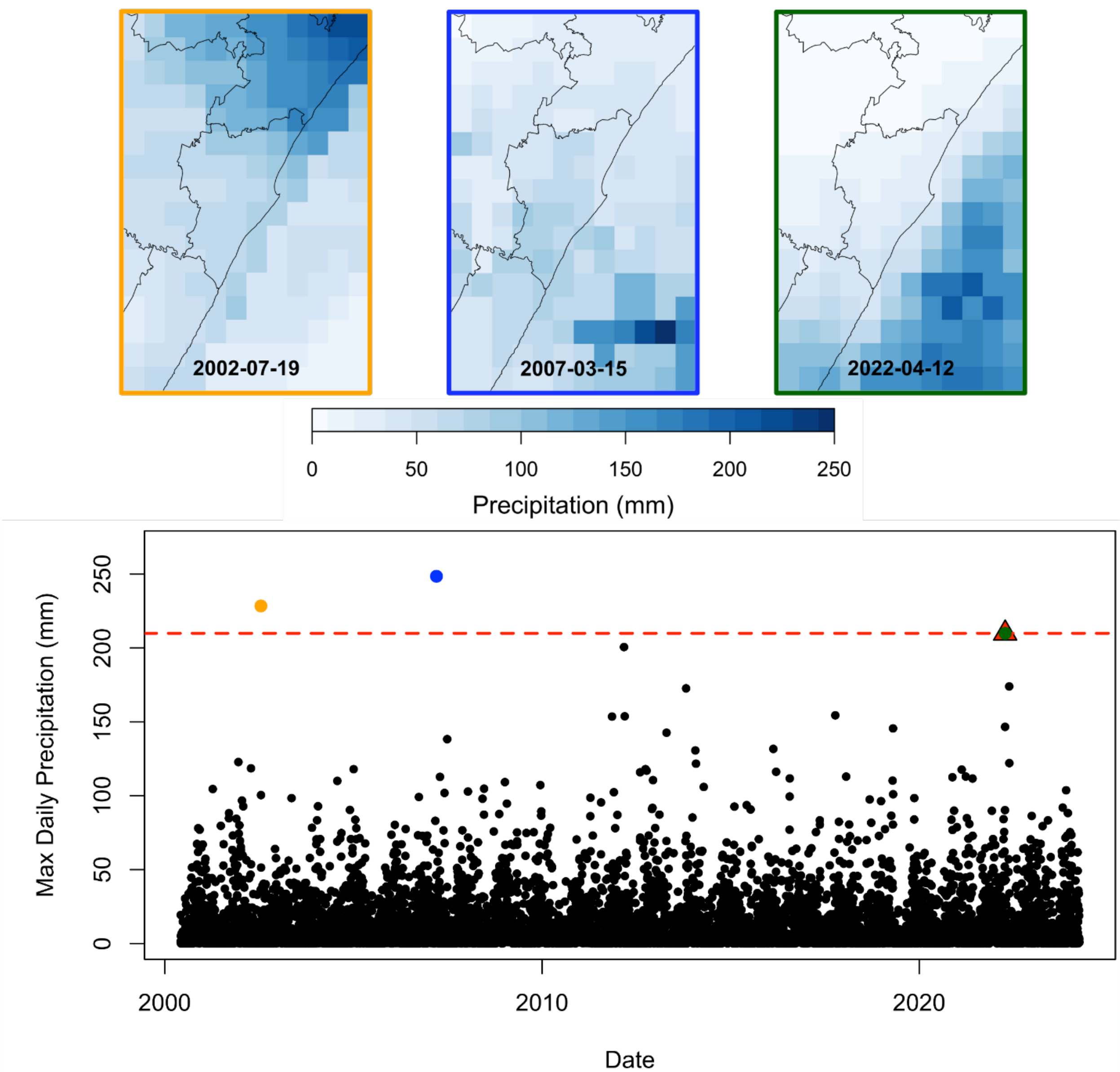

Figure 4. Time series of daily maximum precipitation for the South Africa bounding area with the red dotted line highlighting the maximum precipitation (green dot) within the ± 5 days of the reported event that occurred on the reported event date, the maximum precipitation on the reported event date, 12-Apr-2022. The outline of each map corresponds to the maximum precipitation point on the time series plot below each map. Only the event dates that were equal to or more than the threshold for the event are shown.

3. Results

The newly mapped inventories (shown in **Table 2)** included 15,274 landslide points. Each landslide point in the new event inventories represented one landslide on the ground, as seen in **Figure 5.**

Five landslide events were mapped for April and July, while zero landslide events were mapped for January, June, November, and December (**Figure 6**). Seven of the 22 events were associated with a named storm, but these storms did not necessarily produce more landslides. The inventories for both Tropical Storm Megi and Hurricane Fiona contained fewer than 25 landslides, while some unnamed rainfall events triggered more than 1,000 landslides. Nevertheless, Typhoon Egay and Hurricane Agatha each triggered more than 3,000 landslides. The most common source reporting major landslide events was the IDC (**Figure 6).** Only one new event inventory was automatically digitized, because most landslide events initially seemed small enough to map manually. However, a few events had thousands of landslides; in those instances, it would have been a better use of resources to have utilized SALaD-CD.

Figure 6 shows the climatic variation between the new landslide events mapped using the Koppen-Gieger climate classification (Beck *et al.*, 2023). Most landslides were mapped in the tropical monsoon (Am) and tropical savannah (Aw) climate areas, but many were also mapped in in temperate climates, including Cwa (dry winter, hot summer), Cwb (dry winter, warm summer), and Cfa (no dry season, hot summer).

Event ID	Event Date	# of Landslides Mapped	Province/ Municipality	Country	Associated Storm Name	Mapping Method	Köppen Climate Class
1	23-Apr-2019	57	KwaZulu-Natal	South Africa		Manual	Cfa
2	15-Feb-2022	69	Petrópolis	Brazil		Manual	Cfa, Cfb
3	2-Apr-2022	77	Rio de Janeiro	Brazil		Manual	Af, Am, Cfa, Cfb
4	10-Apr-2022	23	Baybay Village	Philippines	Tropical Storm Megi	Manual	Af

5	12-Apr-2022	870	KwaZulu-Natal	South Africa		Manual	Aw, Cfa
6	22-May-2022	5	KwaZulu-Natal	South Africa		Manual	Cfa
7	28-May-2022	24	Recife	Brazil		Manual	Am, Aw
8	30-May-2022	3,862	Oaxaca	Mexico	Hurricane Agatha	SALaD-CD	Aw, Cwb
9	19-Sep-2022	20	Puerto Rico	United States	Hurricane Fiona	Manual	Af, Cfb
10	28-Oct-2022	213	Maguindanao	Philippines	Tropical Storm Nalgae	Manual	Af
11	19-Feb-2023	330	São Sebãstiao, Ubatuba, and Ilhabela	Brazil		Manual	Af, Cfa, Cfb
12	6-Mar-2023	45	Natuna Regency	Indonesia		Manual	Af
13	13-Mar-2023	1,813	Blantyre, Milange	Malawi, Mozambique	Cyclone Freddy	Manual	Aw, Cwa, Cwb
14	3-Apr-2023	22	Nord-Kivu	Democratic Republic of the Congo		Manual	Af, Am, Cfb
15	2-May-2023	156	Western Province	Rwanda		Manual	Aw, Csb
16	9-Jul-2023	176	Himachal Pradesh	India		Manual	Cwa
17	15-Jul-2023	159	Kyeongbuk Province	South Korea		Manual	Dwa
18	17-Jul-2023	48	Quetame	Colombia		Manual	Af, Am, Csb, Cfb
19	26-Jul-2023	3,183	Cordillera Admin Region	Philippines	Typhoon Egay	Manual	Af, Am, Cwa, Cwb, Cfa, Cfb
20	28-Jul-2023	361	Quanzhou	China	Typhoon Doksuri	Manual	Cfa

21	5-Aug-2023	1,950	Dien Bien, Lai Chau, Son La, Lao Cai, Yen Bai	Vietnam		Manual	Cwa, Cwb
22	6-Aug-2023	1,811	Chittagong	Bangladesh		Manual	Am, Cwa

Table 2. The 22 new landslide events. Dates were reported in the local time zone.

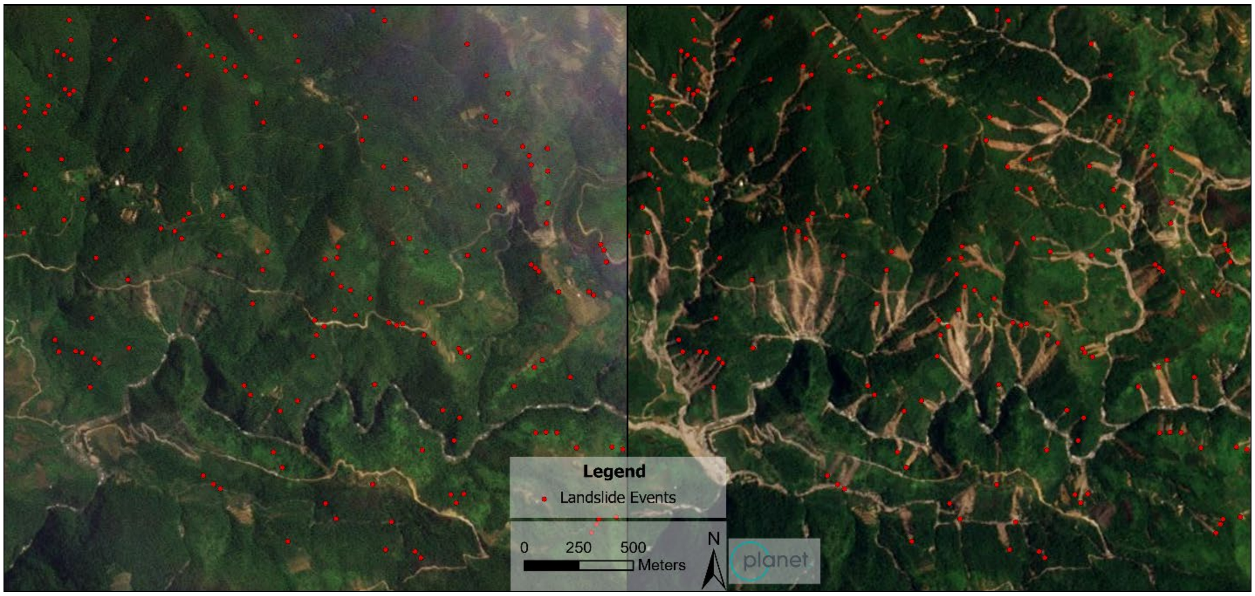

Figure 5. PlanetScope imagery from 17-Jul-2023 (left) and 31-Aug-2023 (right) showing landslide event points from a rainfall event in Vietnam (5-Aug-2023). Located at 21° 47’ 38.19” N 103° 57’ 05.05”E. Image © 2023 Planet Labs PBC.

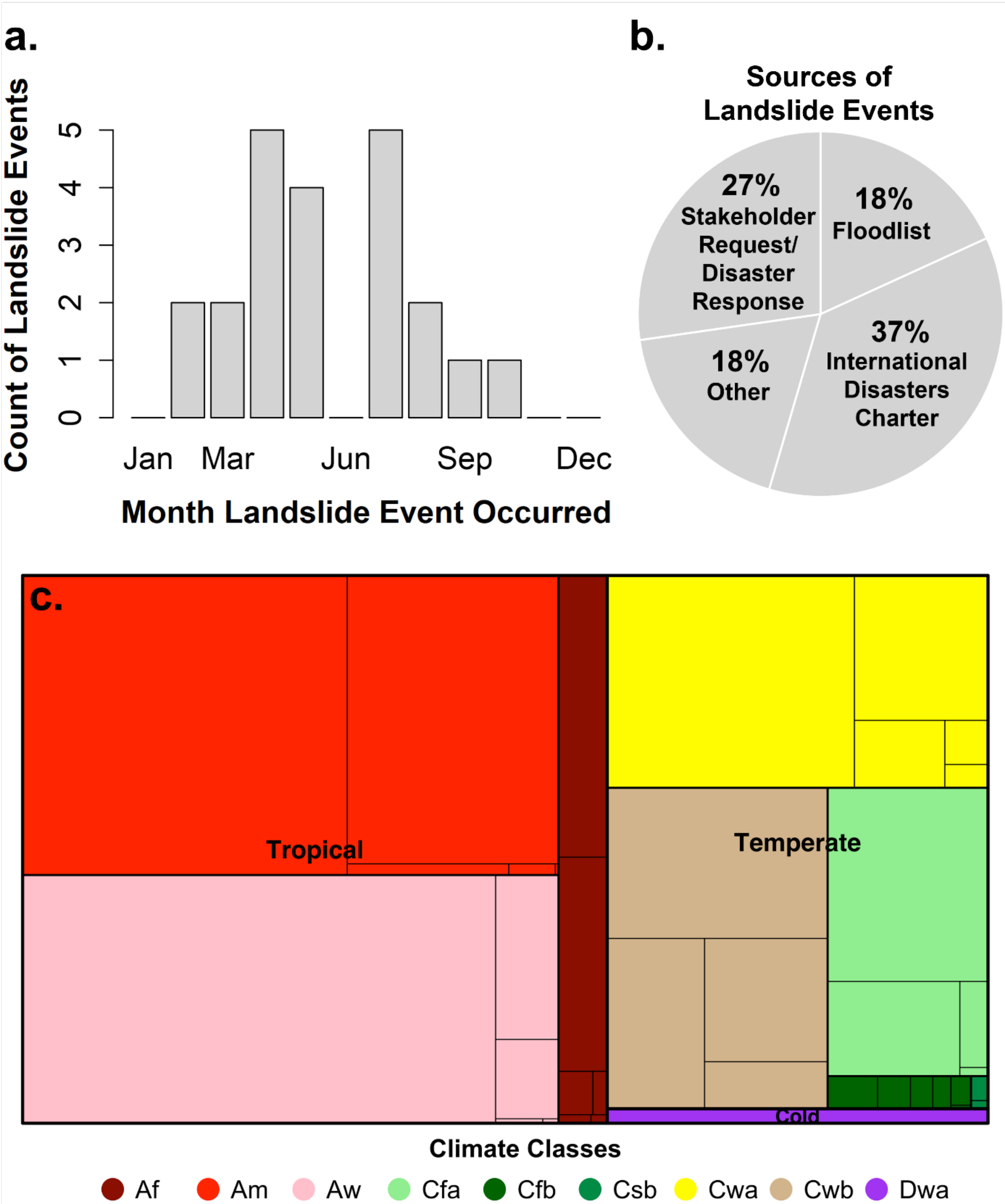

Figure 6. Inset A shows landslide event distribution by month. Inset B shows the different types of sources used to identify the presence of a rainfall-induced landslide event, triggering the landslide mapping process. "Other" includes a variety of news articles. Inset C shows a treemap of the number of landslides by inventory and Koppen-Gieger climate classification (Beck *et al.*, 2023). Each subgroup represents the number of landslides within the climate class for each landslide event inventory. Several landslide events that occurred during a single event were geographically located across multiple climate classes.

Section 2.3. describes an example use case for these inventories. The recurring interval using the maximum daily cumulative precipitation varied from 15 days for the Colombia (17-Jul-2023) landslide event to more than 11 years for the Indonesia (6-Mar-2023) landslide event (**Table 3**) with the average recurring interval for all events being 3.1 years. All the precipitation events had percentile ranks more than the 93rd percentile of all maximum cumulative daily precipitation. Furthermore, 86% of the precipitation events had percentile ranks of more than the 99th percentile for the location. This means that 19 of 22 landslide events had precipitation higher than 99% of all maximum cumulative daily precipitation recorded by GPM IMERG for the study area. According to daily IMERG, eighteen events had the most precipitation fall the day before, on the reported event date, or the day following the reported event date. Three of the twenty-two events had the most precipitation fall more than one day before the reported event. Interestingly, one event had the highest precipitation fall five days following the reported event, Brazil (15-Feb-2022). This suggests that IMERG underestimated the rainfall for the event. According to Alcantara et al. (2023), a strong mesoscale convective system produced rainfall of 258 mm within 3 hours on February 15, 2022, but the maximum daily IMERG precipitation was less than 20 mm on 15-Feb-2022. Additional analysis using the sub-daily precipitation estimates from IMERG did not yield better results for the Brazil event. While the 30-minute IMERG precipitation observed the storm event, the estimated precipitation was much lower than the radar or gauge precipitation presented in Alcantara et al. (2023). The event with the longest recurring interval, the Indonesia event (6-Mar-2023), is discussed in more detail below.

Country	Event Date	Date of Maximum Precipitation (mm/day)	Maximum Precipitation (mm/day)	Number of Days	Recurring Interval (years)
South Africa	23-Apr-2019	22-Apr-2019	73.5	14	1.64
Brazil	15-Feb-2022	20-Feb-2022	22.0	524	0.05
Brazil	02-Apr-2022	1-Apr-2022	133.1	8	3.05
Philippines	10-Apr-2022	10-Apr-2022	186.8	14	1.63
South Africa	12-Apr-2022	12-Apr-2022	209.9	3	9.87
South Africa	22-May-2022	21-May-2022	110.5	5	4.96
Brazil	28-May-2022	25-May-2022	143.6	14	1.69
Mexico	30-May-2022	30-May-2022	148.3	2	5.00
Puerto Rico	19-Sep-2022	18-Sep-2022	188.0	5	4.86
Philippines	28-Oct-2022	27-Oct-2022	119.5	9	2.52

Brazil	19-Feb-2023	19-Feb-2023	97.3	19	1.29
Indonesia	6-Mar-2023	3-Mar-2023	286.9	3	11.05
Malawi, Mozambique	13-Mar-2023	13-Mar-2023	168.3	4	6.68
Congo	3-Apr-2023	31-Mar-2023	26.7	152	0.16
Rwanda	2-May-2023	2-May-2023	62.3	29	0.80
India	9-Jul-2023	8-Jul-2023	155.2	16	1.53
South Korea	15-Jul-2023	14-Jul-2023	105.9	37	0.64
Colombia	17-Jul-2023	17-Jul-2023	32.6	557	0.04
Philippines	26-Jul-2023	26-Jul-2023	317.8	7	3.18
China	28-Jul-2023	28-Jul-2023	89.6	45	0.53
Vietnam	5-Aug-2023	5-Aug-2023	121.5	94	0.25
Bangladesh	6-Aug-2023	6-Aug-2023	336.9	4	7.02

Table 3. Precipitation for each landslide event, selected from a ten-day window around the reported date.

Indonesia: March 6, 2023

An IDC activation for the 6-Mar-2023 landsliding event stated that at least 15 people died after six days of torrential rains and that seasonal rains and high tides contributed to the flooding and landsliding in the region (*International Disasters Charter*, 2023). This event had the longest recurring interval (**Table 3**). The precipitation that occurred in Indonesia around the 6-Mar-2023 landslide event was the third highest precipitation for the bounding area from 1-Jun-2000 through 31-Mar-2024, according to IMERG V07 (**Figure 7**). On 3-Mar-2023, 286.9 mm of precipitation fell, three days before the reported landslide event date of 6-Mar-2023. The bounding area for the event was limited to six IMERG pixels, all of which contained oceanic and terrestrial areas (**Figure 7**).

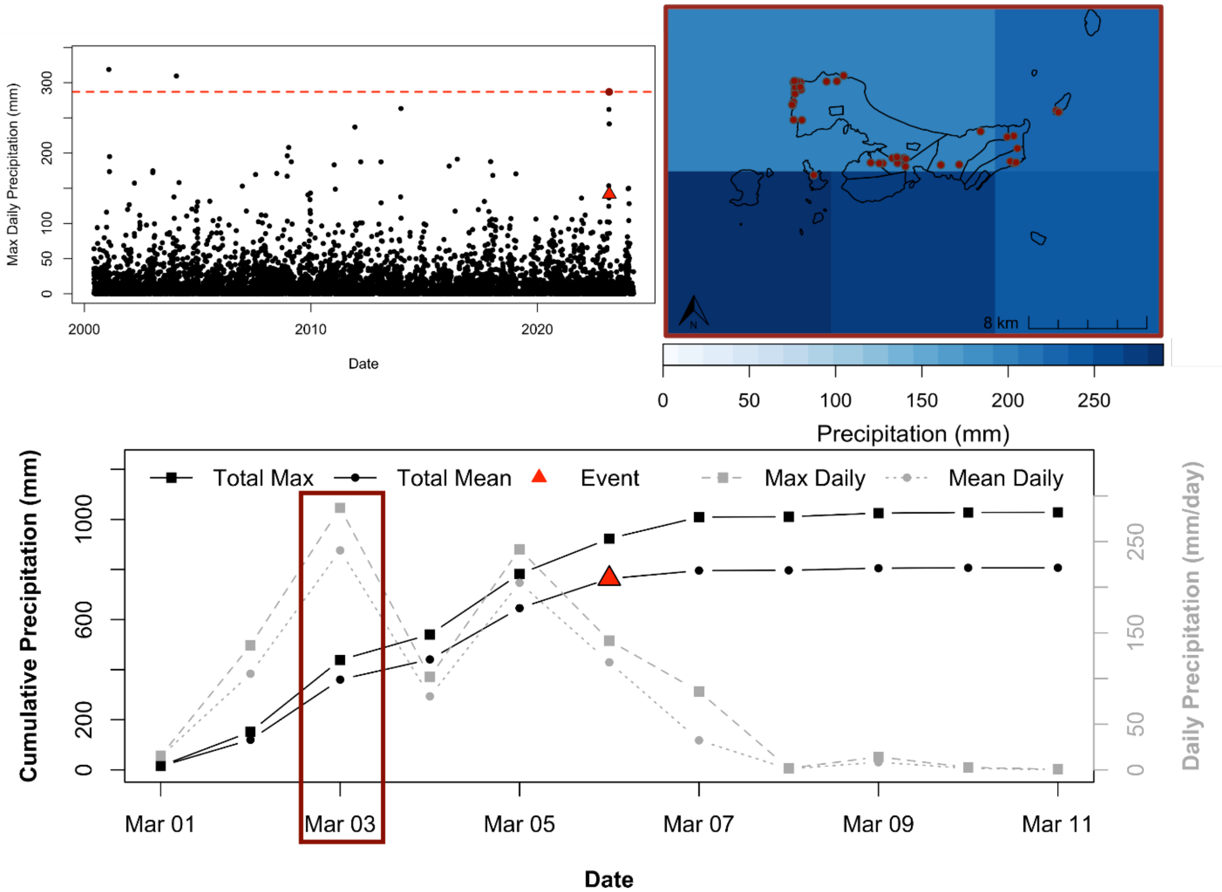

Figure 7. Time series of daily precipitation for the Indonesia event bounding area from 1-Jun-2000 through 31-Mar-2024 (top left). The maximum precipitation occurred three days before the event date on March 3, 2023 (bottom) and is highlighted in the red rectangle in the time series (bottom) and map (top right). Mapped landslides are shown as red dots.

4. Data Availability

The new landslide inventories are available to download in shapefile, csv, and geodatabase format from Landslide Viewer or by going directly to this link: https://maps.nccs.nasa.gov/arcgis/apps/MapAndAppGallery/index.html?appid=574f26408683485799d02e857e5d9521. Landslide Viewer (https://landslides.nasa.gov/viewer) is a web application to visualize and download various landslide-related datasets **(Figure 8)**. It was recently updated with Experience Builder, a tool for building geospatial web applications from Esri. Additional features include aggregation of landslide points, layer reordering, and faster visualization. In addition to landslide inventories, Landslide Viewer also displays information on NASA's global landslide nowcast, a global landslide susceptibility map, precipitation, and infrastructure. To download all the landslide inventories within COOLR, it is recommended to download the geodatabase which contains four layers. In addition, there is a downloadable table which contains the citations for each landslide event inventory. The new landslide event inventories discussed in this paper can also be downloaded from Figshare (https://doi.org/10.6084/m9.figshare.26972467).

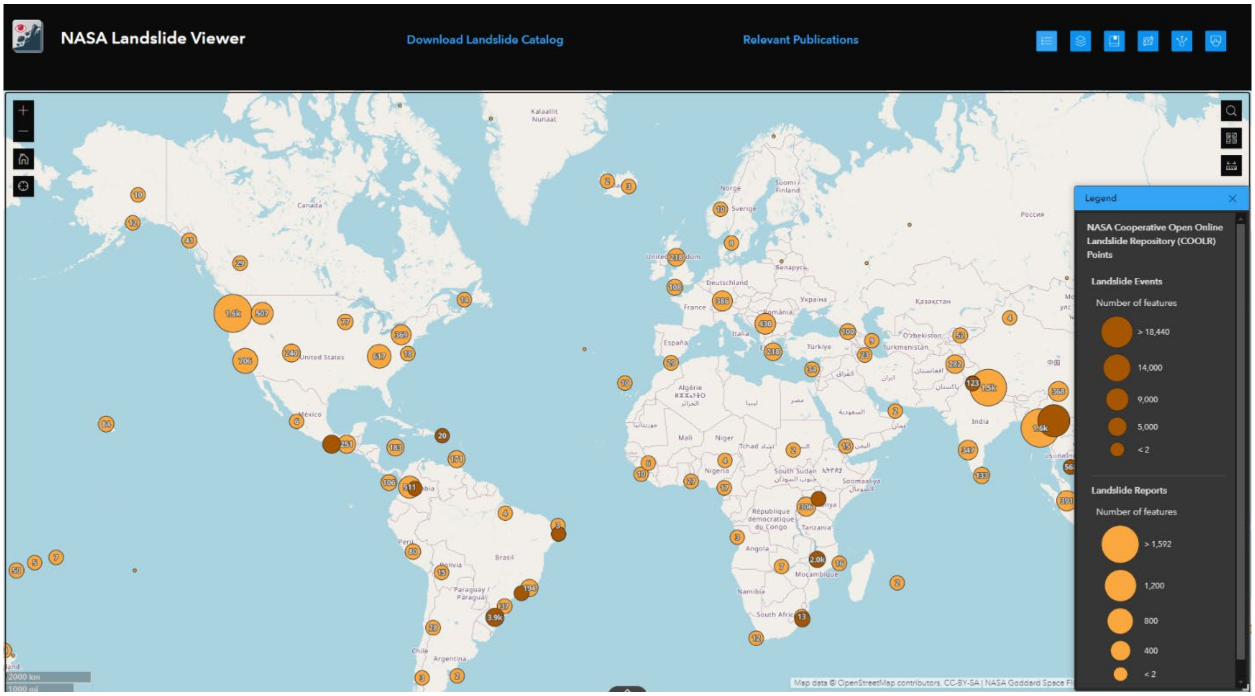

Figure 8. NASA's Landslide Viewer. The "Download Landslide Catalog" and "Relevant Publications" links are shown at the top of the page.

5. Data Use and Reuse

The new landslide event inventories could be used for a multitude of analyses, but they have some important limitations. For example, they can be used to train and validate machine-learning models like SALaD-CD and LHASA or assess satellite-based precipitation algorithms such as IMERG. Most of these inventories were manually mapped using 3-meter optical imagery, so the inventories will not include the smallest landslides. We used a cloud filter of 30% to remove cloud-covered imagery, but this does not imply that the inventories are significantly incomplete; all images were manually selected to be favorable for mapping landslides and are unlikely to have major omissions. Wind throw, clouds, tree cover, shadows, and human judgment all contribute to uncertainty in these data. Since the type and date of pre- and post- image used for each inventory is provided in the geodatabase attribute table, users can generally look up the image and review its quality. Although the core areas of impact were thoroughly mapped, it is possible more landslides were present far (>25km) outside of the selected administrative district. Therefore, some landslides may have been missed. We have not conducted a field-based assessment of these inventories, but we welcome feedback from the community and commit to correcting known errors.

These events are a small and unrepresentative sample of global landslide activity. For example, the monthly distribution (**Figure 6**) does not match that seen in other global datasets (Froude and Petley, 2018; Dandridge *et al.*, 2023). Therefore, sole reliance on these data is not recommended for many potential uses, such as the analysis of trends in landslide activity or national hazard-level comparisons. But once these inventories have been combined with additional datasets, some topics may become tractable. To show one example of how these data can be used, we calculated a recurring interval for each event, based on the IMERG record. Typically, the recurring intervals are quite short (<3 years), which suggests that satellite-based precipitation products may underestimate some important storms.

6. Conclusion

We used high-resolution satellite imagery from PlanetScope, manual digitization, and machine learning to create thousands of event-based landslide points. COOLR was updated to incorporate both event- and report-based landslide inventories and is displayed within an updated version of NASA's Landslide Viewer. These point-based inventories are not a representative subset of global landslide occurrence, so some potential uses are unsuitable, including analysis of trends and international landslide distribution. Further precipitation analysis could illuminate antecedent conditions for these landslides. We will continue to update COOLR with new events to maintain an open global landslide repository.

Acknowledgements

This work utilized data made available through the NASA CSDA Program.

Conflict of interests

The authors declare that they have no conflict of interest.

References

Adriano B, Yokoya N, Miura H, Matsuoka M, Koshimura S. 2020. A Semiautomatic Pixel-Object Method for Detecting Landslides Using Multitemporal ALOS-2 Intensity Images. *Remote Sensing*. Multidisciplinary Digital Publishing Institute, 12(3): 561–561.

Alcantara E, Marengo JA, Mantovani J. 2023. Deadly disasters in southeastern South America: flash floods and landslides of February 2022 in Petropolis, Rio de Janeiro. *Natural Hazards Earth System Science*, 23: 1157–1175. https://doi.org/10.5194/nhess-23-1157-2023.

Amatya P, Kirschbaum D, Stanley T. 2019. Use of Very High-Resolution Optical Data for Landslide Mapping and Susceptibility Analysis along the Karnali Highway, Nepal. *Remote Sensing*, 11(19): 2284–2284. https://doi.org/10.3390/rs11192284.

Amatya P, Kirschbaum D, Stanley T. 2021a. Rainfall-induced landslide inventories for Lower Mekong based on Planet imagery and a semi-automatic mapping method. *Geoscience Data Journal*.

Amatya P, Kirschbaum D, Stanley T, Tanyas H. 2021b. Landslide mapping using object-based image analysis and open source tools. *Engineering Geology*, 282: 106000–106000. https://doi.org/10.1016/j.enggeo.2021.106000.

Beck HE, McVicar TR, Vergopolan N. 2023. High-resolution (1 km) Köppen-Geiger maps for 1901–2099 based on constrained CMIP6 projections. *Sci Data*, 10(724). https://doi.org/10.1038/s41597-023-02549-6.

Bhuyan K, Tanyaş H, Nava L, Puliero S, Meena SR, Floris M, van Westen C, Catani F. 2023. Generating multi-temporal landslide inventories through a general deep transfer learning strategy using HR EO data. *Scientific Reports*, 13(1): 162. https://doi.org/10.1038/s41598-022-27352-y.

Borghuis AM, Chang K, Lee HY. 2007. Comparison between automated and manual mapping of typhoon-triggered landslides from SPOT-5 imagery. *International Journal of Remote Sensing*, 28(8): 1843–1856. https://doi.org/10.1080/01431160600935638.

Breiman L. 2001. Random forests. *Machine learning*. Springer, 45(1): 5–32.

Burrows K, Walters RJ, Milledge D, Densmore AL. 2020. A Systematic Exploration of Satellite Radar Coherence Methods for Rapid Landslide Detection. *Nat. Hazards Earth Syst. Sci. Discuss.* Copernicus Publications, 2020: 1–26. https://doi.org/10.5194/nhess-2020-168.

Burrows K, Walters RJ, Milledge D, Spaans K, Densmore AL. 2019. A new method for large-scale landslide classification from satellite radar. *Remote Sensing*. Multidisciplinary Digital Publishing Institute, 11(3): 237–237.

Comaniciu D, Meer P. 2002. Mean shift: A robust approach toward feature space analysis. *IEEE Transactions on Pattern Analysis & Machine Intelligence*, 24(5): 603–619. https://doi.org/10.1109/34.1000236.

Comert R. 2021. Investigation of the Effect of the Dataset Size and Type in the Earthquake-Triggered Landslides Mapping: A Case Study for the 2018 Hokkaido Iburu Landslides. Front. *Frontiers in Earth Science*, 9: 633665–633665. https://doi.org/10.3389/feart.2021.633665.

Dandridge C, Stanley T, Kirschbaum D, Lakshmi V. 2023. Spatial and Temporal Analysis of Global Landslide Reporting Using a Decade of the Global Landslide Catalog. *Sustainability*, 15(4): 3323. https://doi.org/10.3390/su15043323.

Devoli G, Strauch W, Chávez G, Høeg K. 2007. A landslide database for Nicaragua: a tool for landslide-hazard management. *Landslides*, 4(2): 163–176. https://doi.org/10.1007/s10346-006-0074-8.

Esposito G, Marchesini I, Mondini AC, Reichenbach P, Rossi M, Sterlacchini S. 2020. A spaceborne SAR-based procedure to support the detection of landslides. *Nat. Hazards Earth Syst. Sci.* Copernicus Publications, 20(9): 2379–2395. https://doi.org/10.5194/nhess-20-2379-2020.

Froude MJ, Petley DN. 2018. Global fatal landslide occurrence from 2004 to 2016. *Nat. Hazards Earth Syst. Sci.* Copernicus Publications, 18(8): 2161–2181. https://doi.org/10.5194/nhess-18-2161-2018.

Ghorbanzadeh O, Blaschke T, Gholamnia K, Meena RS, Tiede D, Aryal J. 2019. Evaluation of Different Machine Learning Methods and Deep-Learning Convolutional Neural Networks for Landslide Detection. *Remote Sensing*, 11(2): 196–196. https://doi.org/10.3390/rs11020196.

Grignon A, Bobrowsky P, Coultish T. 2004. Landslide database management philosophy in the Geological Survey of Canada. *Proceedings of the 57th Canadian Geotechnical Conference*, 5.

Günther A, Hervás J, Van Den Eeckhaut M, Malet J-P, Reichenbach P. 2014. Synoptic Pan-European Landslide Susceptibility Assessment: The ELSUS 1000 v1 Map. In: Sassa K, Canuti P and Yin Y (eds) *Landslide Science for a Safer Geoenvironment*. Springer International Publishing: Cham, 117–122.

Herrera G, Mateos RM, García-Davalillo JC, Grandjean G, Poyiadji E, Maftei R, Filipciuc T-C, Jemec Auflič M, Jež J, Podolszki L, Trigila A, Iadanza C, Raetzo H, Kociu A, Przyłucka M, Kułak M, Sheehy M, Pellicer XM, McKeown C, Ryan G, Kopačková V, Frei M, Kuhn D, Hermanns RL, Koulermou N, Smith CA, Engdahl M, Buxó P, Gonzalez M, Dashwood C, Reeves H, Cigna F, Liščák P, Pauditš P, Mikulėnas V, Demir V, Raha M, Quental L, Sandić C, Fusi B, Jensen OA. 2018. Landslide databases in the Geological Surveys of Europe. *Landslides*, 15(2): 359–379. https://doi.org/10.1007/s10346-017-0902-z.

Hölbling D, Friedl B, Eisank C. 2015. An object-based approach for semi-automated landslide change detection and attribution of changes to landslide classes in northern Taiwan. *Earth Science Informatics*, 8(2): 327–335. https://doi.org/10.1007/s12145-015-0217-3.

Hölbling D, Füreder P, Antolini F, Cigna F, Casagli N, Lang S. 2012. A semi-automated object-based approach for landslide detection validated by persistent scatterer interferometry measures and landslide inventories. *Remote Sensing*, 4(5): 1310–1336. https://doi.org/10.3390/rs4051310.

Huffman GJ, Stocker EF, Bolvin DT, Nelkin EJ, Tan J. 2023. GPM IMERG Final Precipitation L3 1 day 0.1 degree x 0.1 degree V07. *Goddard Earth Sciences Data and Information Services Center (GES DISC)*. https://doi.org/10.5067/GPM/IMERGDF/DAY/07.

Juang CS, Stanley TA, Kirschbaum DB. 2019. Using citizen science to expand the global map of landslides: Introducing the Cooperative Open Online Landslide Repository (COOLR). *PloS one*. Public Library of Science, 14(7).

Jung J, Yun S-H. 2020. Evaluation of Coherent and Incoherent Landslide Detection Methods Based on Synthetic Aperture Radar for Rapid Response: A Case Study for the 2018 Hokkaido Landslides. *Remote Sensing*, 12(2). https://doi.org/10.3390/rs12020265.

Kirschbaum D, Stanley T, Zhou Y. 2015. Spatial and temporal analysis of a global landslide catalog. *Geomorphology*, 249: 4–15. https://doi.org/10.1016/j.geomorph.2015.03.016.

Landslides in Indonesia. 2023. *International Disasters Charter*.

Lee M. 2023. Heavy rains coming as monsoon front lingers over Korea. *Korea JoongAng Daily*.

Li G, West AJ, Densmore AL, Jin Z, Parker RN, Hilton RG. 2014. Seismic mountain building: Landslides associated with the 2008 Wenchuan earthquake in the context of a generalized model for earthquake volume balance. *Geochemistry, Geophysics, Geosystems*. \, 15(4): 833–944. https://doi.org/10.1002/2013GC005067.

Lu P, Stumpf A, Kerle N, Casagli N. 2011. Object-oriented change detection for landslide rapid mapping. *IEEE Geoscience and remote sensing letters*, 8(4): 701–705. https://doi.org/10.1109/LGRS.2010.2101045.

Martha TR, Kamala P, Jose J, Vinod Kumar K, Jai Sankar G. 2016. Identification of new Landslides from High Resolution Satellite Data Covering a Large Area Using Object-Based Change Detection Methods. *Journal of the Indian Society of Remote Sensing*, 44(4): 515–524. https://doi.org/10.1007/s12524-015-0532-7.

Martha TR, Kerle N, Jetten V, van Westen CJ, Kumar KV. 2010. Characterising spectral, spatial and morphometric properties of landslides for semi-automatic detection using object-oriented methods. *Geomorphology*, 116(1–2): 24–36. https://doi.org/10.1016/j.geomorph.2009.10.004.

Meena SR, Ghorbanzadeh O, van Westen CJ, Nachappa TG, Blaschke T, Singh RP, Sarkar R. 2021. Rapid mapping of landslides in the Western Ghats (India) triggered by 2018 extreme monsoon rainfall using a deep learning approach. *Landslides*, 1–14. https://doi.org/10.1007/s10346-020-01602-4.

Mirus BB, Jones ES, Baum RL, Godt JW, Slaughter S, Crawford MM, Lancaster J, Stanley T, Kirschbaum DB, Burns WJ, Schmitt RG, Lindsey KO, McCoy KM. 2020. Landslides across the USA: occurrence, susceptibility, and data limitations. *Landslides*, 17(10): 2271–2285. https://doi.org/10.1007/s10346-020-01424-4.

NASA JPL. 2020. NASADEM Merged DEM Global 1 arc second V001 [Data set]. *NASA EOSDIS Land Processes DAAC*. https://doi.org/10.5067/MEaSUREs/NASADEM/NASADEM_HGT.001.

Nava L, Bhuyan K, Meena SR, Monserrat O, Catani F. 2022. Rapid Mapping of Landslides on SAR Data by Attention U-Net. *Remote Sensing*. MDPI, 14(6): 1449–1449.

Nichol J, Wong MS. 2005. Satellite remote sensing for detailed landslide inventories using change detection and image fusion. *International journal of remote sensing*, 26(9): 1913–1926. https://doi.org/10.1080/01431160512331314047.

Parker RN, Densmore AL, Rosser NJ, De Michele M, Li Y, Huang R, Whadcoat S, Petley DN. 2011. Mass wasting triggered by the 2008 Wenchuan earthquake is greater than orogenic growth. *Nature Geoscience*. Nature Publishing Group, 4(7): 449–452.

Perica SS, Pavlovic M, St. Laurent C, Trypaluk D, Unruh O, Whilhite. 2018. Precipitation-Frequency Atlas of the United States, Texas. NOAA, National Weather Service: Silver Spring, MD.

Planet Team. 2017. Planet Application Program Interface: In Space for Life on Earth. San Francisco, CA. .

R Core Team. 2024. R Core Team.

Sameen MI, Pradhan B. 2019. Landslide detection using residual networks and the fusion of spectral and topographic information. *IEEE Access*, 7: 114363–114373. https://doi.org/10.1109/ACCESS.2019.2935761.

Stanley TA, Kirschbaum DB, Benz G, Emberson RA, Amatya PM, Medwedeff W, Clark MK. 2021. Data-Driven Landslide Nowcasting at the Global Scale. *Frontiers in Earth Science*, 9: 378–378. https://doi.org/10.3389/feart.2021.640043.

Stumpf A, Kerle N. 2011. Object-oriented mapping of landslides using Random Forests. *Remote Sensing of Environment*, 115(10): 2564–2577. https://doi.org/10.1016/j.rse.2011.05.013.

Tanyaş H, Van Westen CJ, Allstadt KE, Anna Nowicki Jessee M, Görüm T, Jibson RW, Godt JW, Sato HP, Schmitt RG, Marc O, Hovius N. 2017. Presentation and Analysis of a Worldwide Database of Earthquake-Induced Landslide Inventories. *Journal of Geophysical Research: Earth Surface*, 122(10): 1991–2015. https://doi.org/10.1002/2017JF004236.

Trigila A, Iadanza C, Spizzichino D. 2010. Quality assessment of the Italian Landslide Inventory using GIS processing. *Landslides*, 7(4): 455–470. https://doi.org/10.1007/s10346-010-0213-0.

Wilde M, Günther A, Reichenbach P, Malet J-P, Hervás J. 2018. Pan-European landslide susceptibility mapping: ELSUS Version 2. *Journal of Maps*, 14(2): 97–104. https://doi.org/10.1080/17445647.2018.1432511.